Journal of Materials Science: Materials in Electronics (2018) 29:20991–21001
https://doi.org/10.1007/s10854-018-0244-1

Heteroatoms (O, N)-doped porous carbon derived from bamboo shoots shells for high performance supercapacitors

Junjian Han[1] · Qiang Li[1] · Jiaqi Wang[1] · Jianglin Ye[2] · Guangsheng Fu[1] · Lei Zhai[3] · Yanwu Zhu[2]

Received: 5 June 2018 / Accepted: 17 October 2018 / Published online: 29 October 2018

Abstract
Activated carbon derived from plant wastes is attractive for the fabrication of low cost and high performance electrochemical energy storage devices. The heteroatoms (O, N)-doped porous carbon (KAC-700) is fabricated from bamboo shoots shells via KOH activation. The symmetric supercapacitor based on KAC-700 has gravimetric and volumetric capacitance of 223.21 F g^{-1} and 167.63 F cm^{-3}, respectively, at current density of 1 A g^{-1} in 1 M H_2SO_4 electrolyte. This supercapacitor also delivers a high energy density of 13.15 Wh kg^{-1} at power density of 546.60 W kg^{-1} in 1 M Na_2SO_4 electrolyte, as well as high capacitance retention rate of 93.62% after 4000 cycles at 5 A g^{-1}. Compared with graphene, carbon nanotubes and other expensive carbon material, this activated carbon has a bright future due to its low cost and easy fabrication process as electrode material for supercapacitors.

1 Introduction

Supercapacitors have attracted extensive attention as efficient energy storage devices due to the characteristics of large capacity, fast charging and good cycle stability [1–3]. Supercapacitors can be divided into two types according to the different energy storage mechanism. One is carbon-based double-layer supercapacitor, which stores and releases charges through the electrostatic interaction between electrode materials and electrolyte. Another one is electrochemical capacitor, the pseudocapacitor, which stores the charge by the oxidation–reduction reaction on the electrode surface [4–6]. Pseudocapacitor electrode materials mainly include metal oxides and conductive polymers, such as MnO_2 [7], V_2O_5 [8], Prussian blue [9], PPy [10], PANI [11]. Carbon materials [3, 12] are most common electrode materials for supercapacitors because of their stable chemical properties, ease of building stable bilayer structures, larger specific surface area (SSA) with hierarchical pores through pore structure engineering, high electrical conductivity and good compatibility with other composite materials. For example, sheet-like nanocarbon fabricated from graphene oxide and a polytetrafluoroethylene (PTFE) polymer shows excellent electrochemical performance [13]. A hybrid supercapacitor using porous graphene nanosheet as negative electrode gives a high energy density of 50.0 Wh kg^{-1} with power density of 467 W kg^{-1} [14]. While significant effort has been devoted to produce various carbon electrode materials including activated carbon [12, 15], carbon nanotubes [13], and graphene [14], activated carbon is the preferred choice for commercial supercapacitor due to the low preparation cost.

Carbon precursors with high carbon content like fossil fuels [16], polymers [17], and biomass materials [12] are usually used to produce activated carbon. Among them, the plant wastes, as a kind of biomass materials, are of particular interest because they are cheap, easily available and environment friendly. Some of the plant wastes being exploited are wild jujube [12], soybean residue [18], pomelo peels [19], banana peels [20], lotus stems and leaves [21], celtuce leaves [22] and willow catkins [23]. The fabrication of activated carbon from plant wastes usually involves two steps, carbonization and activation by zinc chloride [24, 25], potassium hydroxide [14, 26], phosphoric acid [27], or other

✉ Qiang Li
qli@hfut.edu.cn

✉ Yanwu Zhu
zhuyanwu@ustc.edu.cn

[1] School of Electronic Science and Applied Physics, Hefei University of Technology, Hefei 230009, Anhui, China

[2] Department of Materials Science and Engineering, University of Science and Technology of China, Hefei 230026, Anhui, China

[3] NanoScience Technology Center and Department of Chemistry, University of Central Florida, 12424 Research Parkway, Suite 400, Orlando, FL 32826, USA

activators [28, 29]. For most activated carbon derived from biomass precursors, the fabrication processes are relatively complex and time-consuming. Therefore, it is still a challenge to explore effective fabrication methods to obtain biomass based carbon with high electrochemical performance, such as introducing heteroatoms into activated carbon and making it with hierarchical pores.

As a renewable plant waste, bamboo shoots shells have high content in protein, amino acids and carbohydrates which would introduce heteroatoms into the activated carbon final product [30]. These heteroatoms will improve the wettability and electrical conductivity of the carbon electrodes [15]. In this work, activated porous carbon was derived from bamboo shoots shells by using KOH (KAC-700) and $ZnCl_2$ (ZAC-700) as activators through one-step activation method to build hierarchical pores. The two-electrode symmetrical supercapacitors were assembled and tested in different electrolytes. Overall, KAC-700 based supercapacitor electrodes have better electrochemical performance than ZAC-700 based electrodes. In 1 M H_2SO_4 electrolyte, the gravimetric capacitance and volumetric capacitance of KAC-700 are 223.21 F g^{-1} and 167.63 F cm^{-3} at current density of 1 A g^{-1}. The energy density of KAC-700 reaches up to 13.15 Wh kg^{-1} at power density of 546.60 W kg^{-1} in 1 M Na_2SO_4 electrolyte. Meanwhile, it has a high capacitance retention rate of 93.62% after 4000 cycles at 5 A g^{-1} in 1 M Na_2SO_4. The results show that KAC-700 exhibits excellent electrochemical performance as electrode material for supercapacitor.

2 Experimental

2.1 Materials

The bamboo shoots shells were obtained from a supermarket in Hefei. Potassium hydroxide (KOH), zinc chloride ($ZnCl_2$), sulfuric acid (H_2SO_4), sodium sulfate (Na_2SO_4), hydrochloric acid (HCl) and ethanol were analytical pure grade and purchased from Sinopharm Chemical Reagent Co., Ltd. PTFE (60 wt%) was purchased from Sigma-Aldrich. Deionized water was used for all the experiment processes.

2.2 Preparation of activated carbon

Figure 1 illustrates the process of preparing activated carbon by one-step activation. First, the bamboo shoots shells were cut into pieces, followed by ultrasonic cleaning in ethanol and deionized water for 20 min and filtration. Next, the washed material was placed in blast furnace at 60 °C for 24 h and then transferred to a vacuum oven at 110 °C for drying. Finally, the dried material was ground with a ball mill at a speed of 450 r min^{-1} for 8 h. The resulting sample is denoted as Raw-C.

KOH and $ZnCl_2$ were used to activate Raw-C, respectively. 2 g Raw-C was mixed with 2 g KOH (Raw-C:KOH mass ratio of 1:1) and 6 g $ZnCl_2$ (Raw-C:$ZnCl_2$ mass ratio of 1:3) in 40 mL deionized water, respectively. The mixture of Raw-C and KOH was stirred at 80 °C until the water was completely evaporated. The mixture of Raw-C and $ZnCl_2$ was stirred firstly then immersed at room temperature for

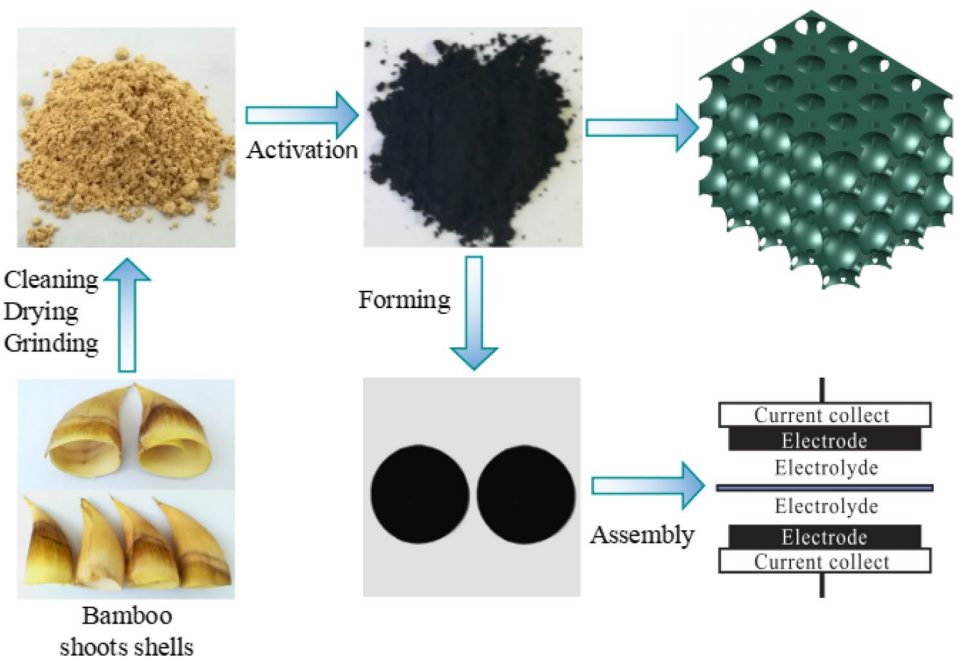

Fig. 1 Schematic of the activated porous carbon derived from bamboo shoots shells for supercapacitor

6 h, and then placed in vacuum oven at 60 °C to evaporate water. The two dried mixtures were both activated in tube furnace under N_2 flow (heating rate is 10 °C min^{-1} from room temperature to 700 °C and gas flow rate is 50 mL min^{-1}) and held at 700 °C for 2 h, respectively. The obtained materials were washed with 1 M HCl and deionized water until the pH was adjusted to 7. The resulting samples are denoted as KAC-700 (KOH activation) and ZAC-700 ($ZnCl_2$ activation).

For comparison, Raw-C was carbonized directly in the same heat treatment condition as above, and the sample was denoted as AC-700.

2.3 Structural characterizations

Morphologies and microstructures of the samples were examined with field emission scanning electron microscope (FE SEM, SU8020) and high-resolution transmission electron microscope (HRTEM, JEOL-2100), respectively. Pore size characteristics of the samples were investigated by a pore size analyzer (Autosorb iQ) at 77 K. The SSA and pore size distribution of the samples were calculated by the Brunauer–Emmett–Teller (BET) method and the quenched solid density functional theory method from N_2 adsorption–desorption isotherms, respectively. The surface functional groups, elemental components, and chemical states of the sample material were analyzed by X-ray photoelectron spectroscopy (XPS, Perkin-Elmer, ESCALAB 250). The composition and crystal structure of the material were analyzed by X-ray diffraction (XRD, ESCALAB 250xi) with Bragg's angle (2θ) range from 10° to 80°.

2.4 Electrochemical measurements

Activated carbon, acetylene black and PTFE were mixed thoroughly with a weight ratio of 80:15:5 then rolled into a sheet (The thickness is about 40 μm.). Round discs with a diameter of 9 mm (The mass and thickness of a single electrode are about 1.45–2.05 mg and 40 μm, respectively.) were punched out from the sheet to build supercapacitor electrode. Two electrodes were assembled into a symmetrical supercapacitor. The electrochemical performances of the samples were measured in two-electrode symmetrical supercapacitor. The electrolytes were 1 M H_2SO_4 and 1 M Na_2SO_4, respectively. The cyclic voltammetry (CV), constant current charge and discharge (GCD) and electrochemical impedance spectroscopy (EIS) measurements were performed on electrochemical workstation (CHI660E, Chenhua Instruments, China). The electrochemical properties of the electrode materials were analyzed by CV (various scan rates from 0.5 to 0.01 V s^{-1}), GCD (various current densities from 30 to 1 A g^{-1}) and EIS curves (The frequency range is 0.01 Hz–100 kHz).

The gravimetric capacitance (C_g, F g^{-1}) and volumetric capacitance (C_v, F cm^{-3}) of the samples based on the GCD curves were calculated by the following equation [12, 31]:

$$C_g = \frac{4I \times dt}{m \times dU} \tag{1}$$

$$C_v = C_g \times \rho \tag{2}$$

$$\rho = m/V \tag{3}$$

$$V = \pi \times r^2 \times h \tag{4}$$

where I (A) is the constant discharging current, m (g), dU (V) and ρ (g cm^{-3}) are the mass of total active material, voltage change (IR drop was excluded) within the discharge time (dt (s)) and density of individual electrode, respectively. V (cm^3), r (cm) and h (cm) are the volume, radius and thickness of the electrodes, respectively.

The energy density (E, Wh Kg^{-1}) and power density (P, W Kg^{-1}) of the samples were calculated according to [31]:

$$E = \frac{1}{8} \times \frac{1}{3.6} \times C_g U^2 \tag{5}$$

$$P = \frac{E}{t} \times 3600 \tag{6}$$

where C_g (F g^{-1}) is the specific capacitance, U (V) is the cell voltage for charging and discharging (IR drop was excluded), and t (s) is the discharge time.

3 Results and discussion

3.1 Characterization

Figure 2 shows the surface morphologies and microstructures of the samples. The SEM of AC-700 shows the form of irregular sheet or flake, which is just carbonized and not activated (Fig. 2a). The activated sample material (ZAC-700 and KAC-700) has a significant difference from AC-700. There are some obvious irregular particles on the ZAC-700 as shown in Fig. 2c. In contrast, KAC-700 has mainly porous honeycomb structures (Figs. 1, 2b). This porous structure for KAC-700 can store electrolytes and form a three-dimensional channel for ion transport, which is more conducive to the diffusion and transport of electrolyte ions. HRTEM images (Fig. 2d–f) clearly show the disordered slit-like pattern, indicating that the prepared samples are mainly composed of amorphous carbon, which is also confirmed by XRD inspection.

Figure 3 shows the N_2 adsorption and desorption isotherms and pore size distributions of KAC-700 and ZAC-700. Figure 3a, c show that the two samples have the I/

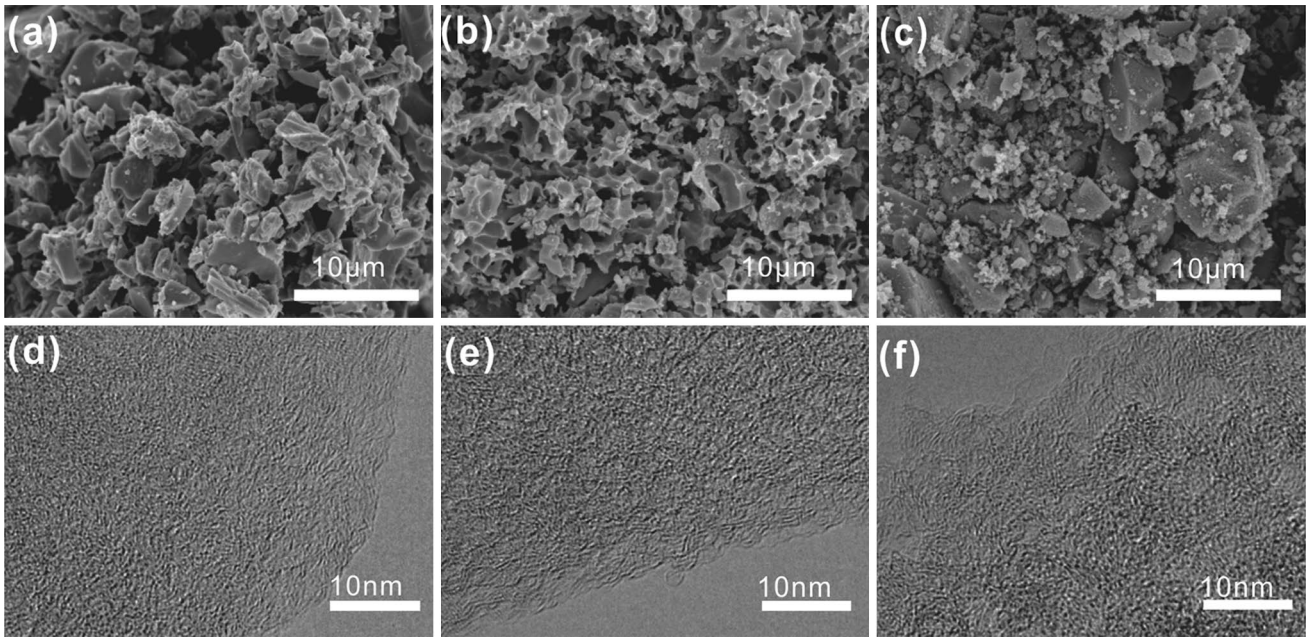

Fig. 2 **a** SEM and **d** TEM images of AC-700. **b** SEM and **e** TEM images of KAC-700. **c** SEM and **f** TEM images of ZAC-700

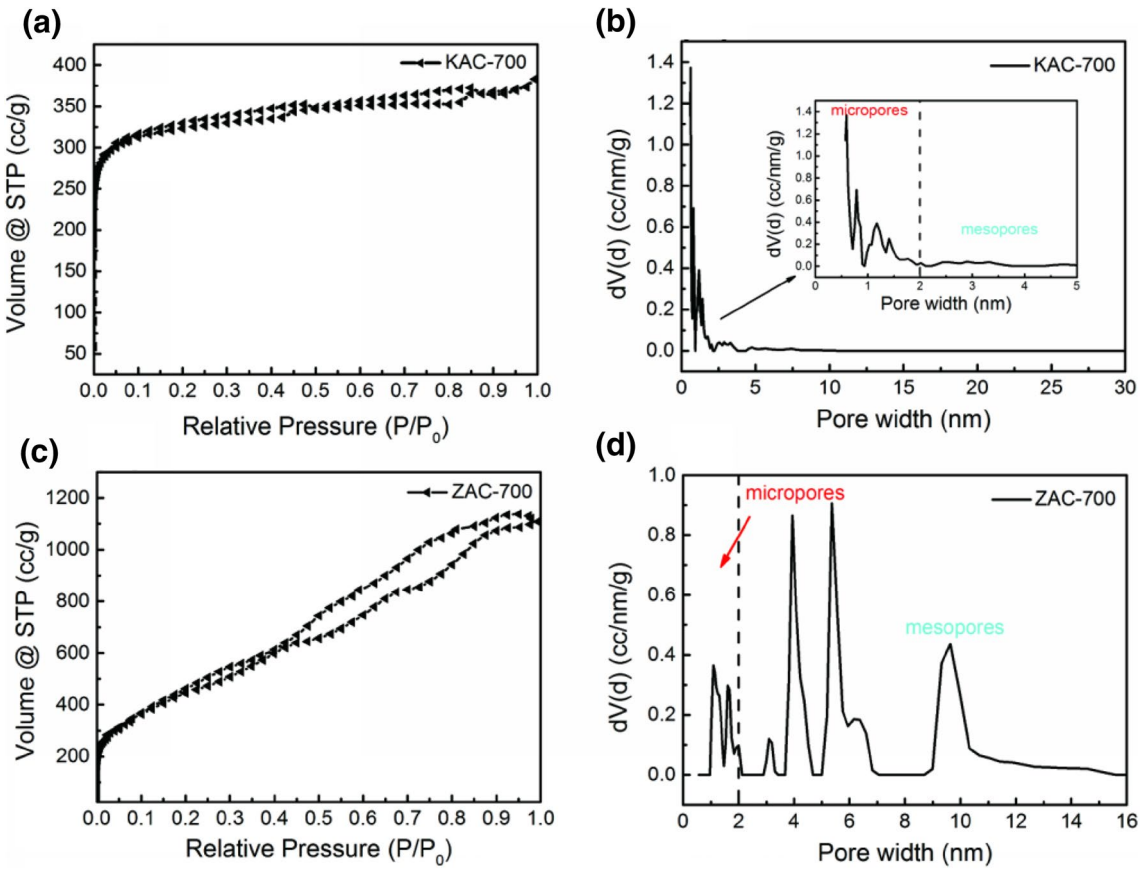

Fig. 3 **a, c** N_2 adsorption and desorption isotherms, **b, d** pore size distribution of KAC-700 and ZAC-700

IV-type N_2 adsorption–desorption isotherm with a significant hysteresis loop, indicating the existence of abundant micropores and mesopores in them [32, 33]. However, the pore size distribution of KAC-700 is different from that of ZAC-700. There are mainly micropores and few mesopores in KAC-700 (Fig. 3b), but ZAC-700 has more mesopores than micropores (Fig. 3d). The SSA and the pore volume of KAC-700 and ZAC-700 were obtained by BET method from N_2 adsorption–desorption isotherm, as shown in Table 1. KAC-700 has SSA of 1351 $m^2\ g^{-1}$ ($S_{micro} = 1309\ m^2\ g^{-1}$, $S_{meso/macro} = 42\ m^2\ g^{-1}$), and ZAC-700 has SSA of 1189 $m^2\ g^{-1}$ ($S_{micro} = 526\ m^2\ g^{-1}$, $S_{meso/macro} = 663\ m^2\ g^{-1}$). The pore volume of KAC-700 is 0.533 $cm^3\ g^{-1}$, and it is 1.675 $cm^3\ g^{-1}$ for ZAC-700. The pore size distribution of activated carbon has great influence on its specific capacitance. Usually, the electric double-layer capacitance (EDLC) of activated carbon is mainly determined by the micropores, and the meso/macropores will influence its rate capability [34, 35]. Therefore, the difference of pore size distribution of KAC-700 and ZAC-700 would affect their electrochemical performance.

Figure 4a shows the XRD pattern of the samples. Both AC-700 and ZAC-700 have two broad diffraction peaks concentrated at 23° and 43.8°, respectively. However, KAC-700 only has a weak diffraction peak at 23°. The peaks at 23° and 43.8° indicate the (002) diffraction of inorganic carbon and the (100) diffraction of graphitized carbon, respectively [36]. Therefore, KOH activation would make the activated carbon more amorphous. The Raman spectra of the samples show two different peaks located at 1338 and 1589 cm^{-1} (Fig. 4b), which correspond to the D-band and G-band of the activated carbon, respectively. The D-band indicates the disordered graphite structure, while the G-band indicates the presence of crystalline graphite carbon. D-band and G-band strength ratio (I_D/I_G) can be used to reflect the degree of graphitization of carbon materials [37]. The I_D/I_G ratios of AC-700, ZAC-700 and KAC-700 are 1.01, 1.03 and 1.06, respectively, indicating that KOH activation is more effective in increasing the defects of activated carbon than $ZnCl_2$ activation, which is consistent with the XRD results.

Figure 4c shows the XPS full spectra of the samples. C 1s, O 1s and N 1s peakes can be clearly observed from the graph. The C 1s of the KAC-700 (Fig. 4d) can be deconvoluted into the following five peaks: C=C (Sp2, 284.7 eV, 39.5%), C–C (Sp3, 285.1 eV, 32.7%), C–O (286.4 eV), C=O (287.3 eV) and O=C–O (289.1 eV) [38–41]. It is reported that larger area ratio of Sp2/Sp3 suggested a higher degree of graphitization. Compared with ZAC-700 (Sp2/Sp3 = 0.99), KAC-700 (Sp2/Sp3 = 1.2) has a higher degree of graphitization, which is also demonstrated by Raman spectroscopy [42]. The O 1s of the KAC-700 (Fig. 4e) can be deconvoluted into the following three peaks: C=O (quinone type groups, 531.2 eV), C–O (ether groups, 532.2 eV), O–H (phenol groups, 533.2 eV) [43]. N 1s (Fig. 4f) can be deconvoluted into the following three peaks: pyrrolic-N (N in five-member ring, 399.5 eV), graphitic-N (N in graphene basal plane, 400.7 eV), pyridine-N-oxide (402.5 eV) [44]. It is also reported that the presence of graphitic-N can enhance the conductivity of electrode materials, which is beneficial for rate and cycling performances of supercapacitors [45]. In addition, the nitrogen and oxygen are introduced successfully to change the electron distribution of carbon electrode materials, and to improve the wettability between electrode materials and electrolyte, and also to increase the active surface area of electrolyte [46]. Physical and electrochemical properties of the samples are summarized in Table 2. The BET and XPS results suggest that the surface area and pore feature may have larger effect than heteroatom doping on the capacitance.

3.2 Electrochemical characterization

Electrochemical performances of AC-700, ZAC-700 and KAC-700 in 1 M H_2SO_4 were shown in Fig. 5. Figure 5a shows the CV curves of AC-700, ZAC-700 and KAC-700 at scan rate of 10 mV s^{-1}. It is obvious that the CV curves of ZAC-700 and KAC-700 have rectangular shape with no redox peak, which indicates their good double-layer capacitance performance. Figure 5b shows the GCD curves of C-700, ZAC-700 and KAC-700 at

Table 1 Microporous structures of the ZAC-700 and KAC-700 samples

Sample	S_{BET}[a] ($m^2\ g^{-1}$)	S_{micro}[b] ($m^2\ g^{-1}$)	$S_{meso/macro}$[c] ($m^2\ g^{-1}$)	V_T[d] ($cm^3\ g^{-1}$)	V_{micro}[e] ($cm^3\ g^{-1}$)	$V_{meso/macro}$[f] ($cm^3\ g^{-1}$)
ZAC-700	1189	526	663	1.675	0.264	1.411
KAC-700	1351	1309	42	0.533	0.456	0.077

[a]Specific surface area

[b]t-Plot micropore area

[c]t-Plot external area

[d]Total pore volume

[e]t-Plot micropore volume

[f]t-Plot external volume

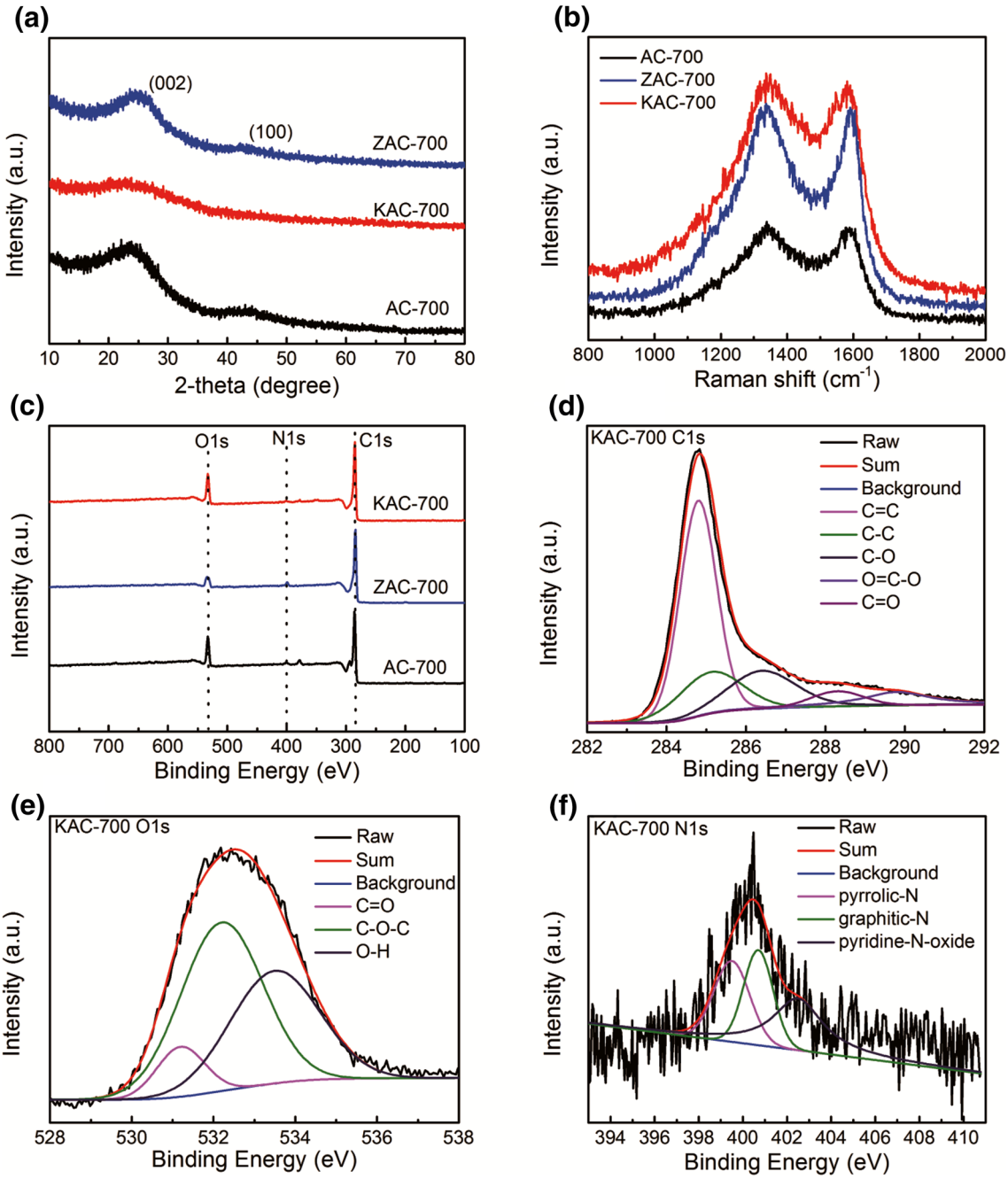

Fig. 4 **a** XRD pattern, **b** Raman spectrum and **c** XPS survey of AC-700, ZAC-700 and KAC-700. **d** C 1s spectra, **e** O 1s spectra and **f** N 1s spectra of KAC-700

Table 2 Physical and electrochemical properties of the samples

Sample	XPS (wt%)			Sp2/Sp3	I_D/I_G	C_g [a] (F g^{-1})	C_v [b] (F cm^{-3})
	C	N	O				
AC-700	80.99	2.07	15.95	0.93	1.01	29.45	7.51
ZAC-700	87.76	4.18	8.06	0.99	1.03	187.97	121.20
KAC-700	82.24	1.9	15.81	1.2	1.06	223.21	167.63

[a]Gravimetric capacitance at 1 A g^{-1}

[b]Volumetric capacitance at 1 A g^{-1}

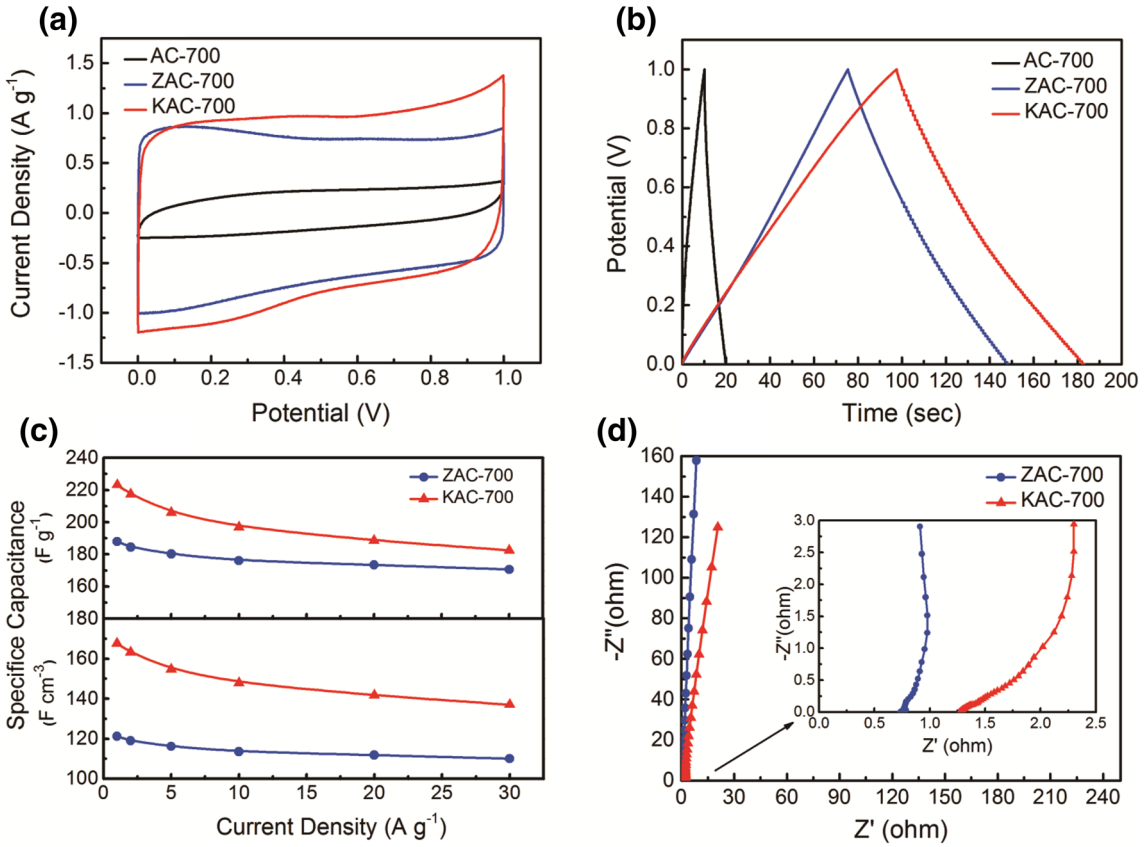

Fig. 5 Electrochemical performance of AC-700, ZAC-700 and KAC-700 measured in 1 M H_2SO_4. **a** CV curves at 10 mV s^{-1}. **b** Galvanostatic charge–discharge curves at 1 A g^{-1}. **c** Gravimetric and volumetric capacitances calculated from the discharge curves under different current densities. **d** Nyquist plots. The inset shows high frequency range

current density of 1 A g^{-1}. They all have an almost symmetrical shape without obvious IR drop, indicating the low series resistance and excellent reversibility of the samples. Both Fig. 5a, b clearly show that ZAC-700 and KAC-700 would give much better capacitive performance than AC-700. The gravimetric and volumetric capacitances of ZAC-700 and KAC-700 were calculated from the galvanostatic discharge curves at different current densities from 1 to 30 A g^{-1} (Fig. 5c). At 1 A g^{-1}, the gravimetric and volumetric capacitances of ZAC-700(ρ: 0.64 g cm^{-3}) are 187.97 F g^{-1} and 121.20 F cm^{-3}, respectively, while KAC-700 (ρ: 0.75 g cm^{-3}) has the gravimetric and volumetric capacitances of 223.21 F g^{-1} and 167.63 F cm^{-3}, respectively (also in Table 2). From 1 to 30 A g^{-1}, the gravimetric capacitance retention of ZAC-700 and KAC-700 can reach 90.70% and 81.80%, respectively. Table 1 show that KAC-700 has higher S_{BET}, S_{micro} and V_{micro}, but lower $S_{meso/macro}$ and $V_{meso/macro}$ than ZAC-700. As for porous carbon, the specific capacitance (EDLC) is mainly determined by the micropores which would provide high SSAs with large active sites for storage of electrolyte ions, and the meso/macropores which would act as electrolyte reservoir to minimize the diffusion resistance and distance of electrolyte ions to the active sites can influence the rate capability of porous carbon [12]. Therefore, on one hand KAC-700 shows higher specific capacitances than ZAC-700 from 1 to 30 A g^{-1}, and on the other hand the rate capability of ZAC-700 is better than that of KAC-700, as shown in Fig. 5c. However, even at high current density of 30 A g^{-1}, KAC-700 still maintains higher capacitances (182.48 F g^{-1} and 137.04 F cm^{-3}) than ZAC-700 (170.57 F g^{-1} and 109.99 F cm^{-3}). Therefore, overall KAC-700 has better capacitive performance than ZAC-700. Furthermore, the high degree of amorphous structure and defects in KAC-700 would also be conducive to the improvement of its capacitance [47]. Figure 5d shows the Nyquist plots of the samples. The nearly vertical lines of ZAC-700 and KAC-700 in the low frequency region indicate their ideal capacitive performance. The intercept of Nyquist plot with real axis illustrates the equivalent serial resistance (R_s) of the electrode. As mentioned above, the meso/macropores would minimize the diffusion resistance and distance of electrolyte ions to the active sites, therefore the symmetric supercapacitor based on ZAC-700

has lower Rs (0.73 Ω) than that on KAC-700 (1.27 Ω), as shown in the inset of Fig. 5d.

A wide operating voltage would help to increase the energy density of supercapacitor. Therefore, the symmetrical supercapacitors based on the ZAC-700 and KAC-700 was tested with 1 M Na_2SO_4 as the electrolyte to increase the operating voltage [48]. The CV curves of ZAC-700 and KAC-700 at 10 mV s^{-1} with voltage window range from 0 to 1.6 V do not change significantly (Fig. 6a). The inset of Fig. 6a shows the CV curves of KAC-700 at different voltage windows. Figure 6b shows the GCD curves of ZAC-700 and KAC-700 at 1 A g^{-1}. The approximate symmetrical triangles with no significant IR drop of the GCD curves indicate the excellent capacitive behavior of ZAC-700 and KAC-700. The gravimetric (volumetric) capacitances of ZAC-700 and KAC-700 at 1 A g^{-1} are 124.38 F g^{-1} (70.91 F cm^{-3}) and 147.93 F g^{-1} (119.23 F cm^{-3}), respectively (Fig. 6c). Even at 30 A g^{-1}, ZAC-700 and KAC-700 still maintain high gravimetric (volumetric) capacitances of 106.9 F g^{-1} (60.94 F cm^{-3}) and 92.58 F g^{-1} (74.62 F cm^{-3}). Compared with some biomass derived carbon, such as Wild jujube pit [12], Soybean residue [18], Lignin [49] and Olive pits [50], KAC-700 has a higher volumetric capacitance, as shown in Table 3. According to the latest reports about N-doped electrodes, such as N-doped mesoporous carbon spheres (The specific capacitance is 231 F g^{-1} at 1 A g^{-1}.) [51] and N-doped carbon nanotubes (The energy density of the HPCNT-SC cell is 8.45 Wh kg^{-1}.) [52], the KAC-700 has certain advantages in terms of electrochemical properties, price and material sources. In Fig. 6d, it can be observed that ZAC-700 and KAC-700 have low R_s of 1.1 Ω and 1.7 Ω, respectively. The almost vertical lines in the low frequency region also illustrate their good capacitance behavior in 1 M Na_2SO_4 electrolytes.

Figure 7a shows the Ragone plot of ZAC-700 and KAC-700 electrodes in 1 M H_2SO_4 and 1 M Na_2SO_4 electrolytes, respectively. Overall, KAC-700 has better electrochemical performance than ZAC-700. KAC-700 has energy density of 7.75 Wh kg^{-1} at a power density of 327.87 W kg^{-1} in 1 M H_2SO_4. Its energy density increases to 13.15 Wh kg^{-1} at a

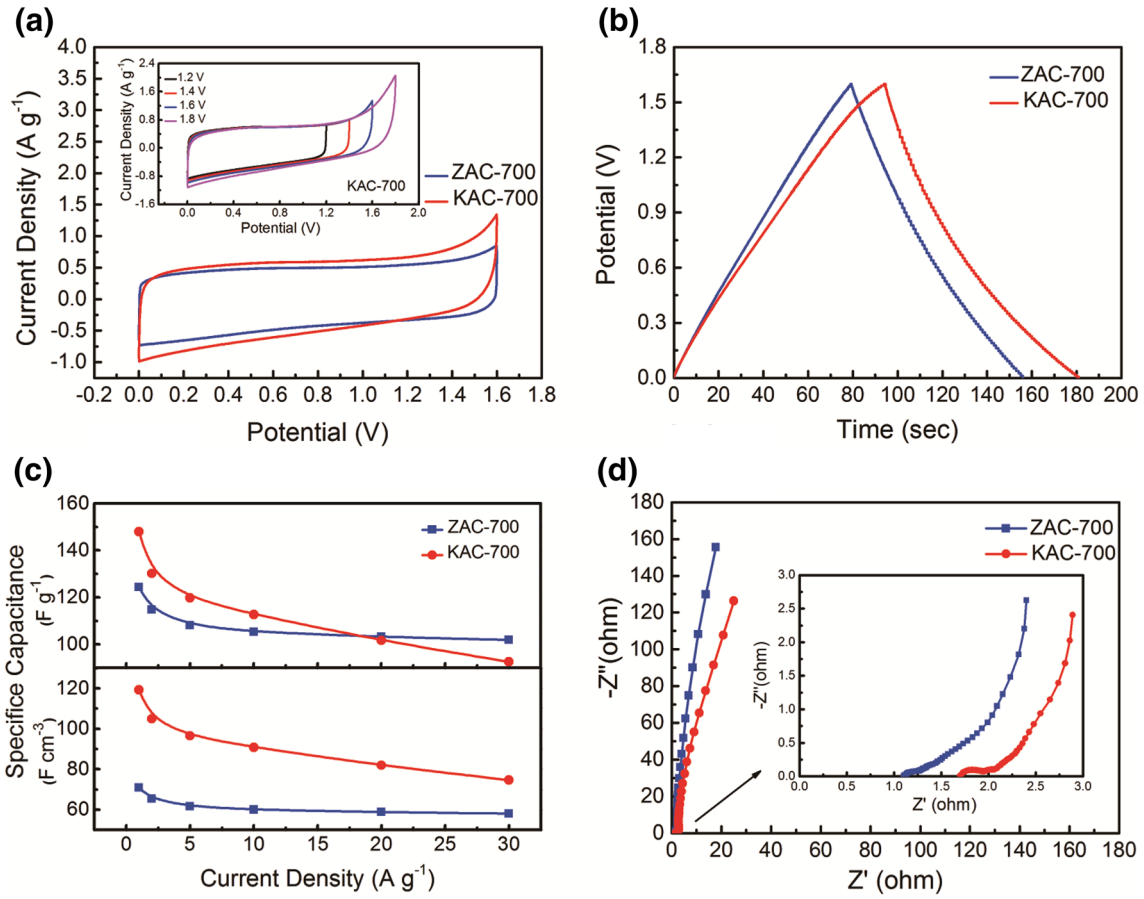

Fig. 6 Electrochemical performance of ZAC-700 and KAC-700 measured in 1 M Na_2SO_4. **a** CV curves at 0.01 V s^{-1}. The inset shows CV curves of KAC-700 at different voltage window at 0.01 V s^{-1}. **b** Galvanostatic charge–discharge curves at 1 A g^{-1}. **c** Gravimetric and volumetric capacitances calculated from the discharge curves under different current densities. **d** Nyquist plots, the inset shows high frequency range

Table 3 Comparison of KAC-700 with the recently reported biomass-based carbon

M[a]	S[b]	C[c] (A g^{-1})	C_v[d] (F cm^{-3})	C_g[e] (F g^{-1})	E[f]	Refs.
Lignin	3E	0.1	97.1	208.4	6 M KOH	[49]
Glucose	3E	0.2	335	386	2 M KOH	[53]
Frutescens	3E	0.5	287	270	6 M KOH	[54]
Seaweed	2E	0.05	208	264	1 M H_2SO_4	[55]
Wild jujube pit	2E	0.5	62.4	260	6 M KOH	[12]
Soybean residue	2E	0.2	150	258	1 M H_2SO_4	[18]
Pomelo peels	2E	0.2	171	342	6 M KOH	[19]
Olive pits	2E	0.5	140	260	6 M KOH	[44]
KAC-700	2E	1.0	167	223	1 M H_2SO_4	This work
		1.0	119	147	1 M Na_2SO_4	

[a]Materials

[b]Two or three electrodes system

[c]Current density (A g^{-1})

[d]Specific volumetric capacitance (F cm^{-3})

[e]Specific gravimetric capacitance (F g^{-1})

[f]Electrolyte

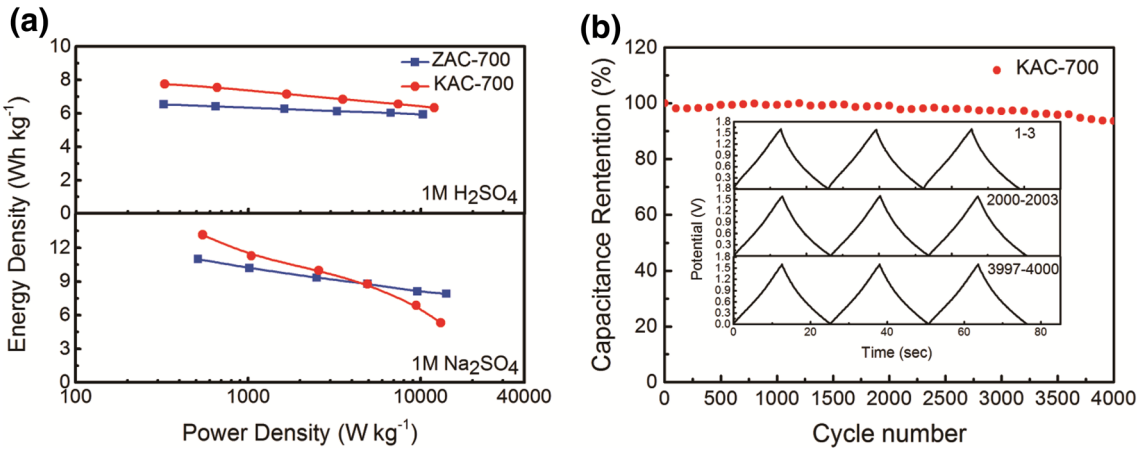

Fig. 7 **a** Ragone plots of ZAC-700 and KAC-700 in 1 M H_2SO_4 and 1 M Na_2SO_4, respectively. **b** Cycling stability of KAC-700 in 1 M Na_2SO_4 for 4000 cycles at 5 A g^{-1}. The inset shows the detailed GCD curves of the start, middle and last three cycles

power density of 546.60 W kg^{-1}, due to a wider operating voltage window in 1 M Na_2SO_4. After 4000 charge–discharge cycles at 5 A g^{-1} in 1 M Na_2SO_4, KAC-700 keeps a high capacitance retention rate of 93.62% (Fig. 7b). There is no significant distortion for the shape of GCD curves during cycling (inset of Fig. 7b), indicating the excellent electrochemical stability of KAC-700. The porous structure of KAC-700 provides more active sites and favorable transport channels for the electrolyte ions.

4 Conclusions

In summary, activated porous carbons were successfully fabricated from bamboo shoots shells via one-step activation by KOH and $ZnCl_2$, respectively. The KAC-700 based symmetric supercapacitor delivers gravimetric and volumetric capacitances of 223.21 F g^{-1} and 167.63 F cm^{-3} at 1 A g^{-1} in 1 M H_2SO_4, and has a high capacitance

retention rate of 81.80% at 30 A g^{-1}. In addition, its energy density is up to 13.15 Wh kg^{-1} at a power density of 546.60 W kg^{-1} in 1 M Na_2SO_4. Meanwhile, KAC-700 has a capacitance retention rate of 93.62% after 4000 cycles at 5 A g^{-1}. Therefore, this activated porous carbon derived from plant waste through simple and scalable technology has excellent electrochemical performance as supercapacitor electrode materials.

Acknowledgements Authors appreciate financial support from the China Government 1000 Plan Talent Program, China MOE NCET Program, Natural Science Foundation of China (51322204), Specialized Research Fund for the Doctoral Program of Higher Education (No. 20120111120009) and Fundamental Research Funds for the Central Universities (WK2060140014, WK2060140017, 2013HGXJ0199, J2014HGXJ0092).

References

1. Q. Wang, J. Yan, J.Z. Fan, Carbon materials for high volumetric performance supercapacitors: design, progress, challenges and opportunities. Energy Environ. Sci. **9**, 729–762 (2016)
2. L. Wang, Y. Han, X. Feng, J. Zhou, P. Qi, B. Wang, Metal–organic frameworks for energy storage: batteries and supercapacitors. Coord. Chem. Rev. **307**, 361–381 (2016)
3. C. Long, D. Qi, T. Wei, J. Yan, L. Jiang, Z. Fan, Nitrogen-doped carbon networks for high energy density supercapacitors derived from polyaniline coated bacterial cellulose. Adv. Funct. Mater. **24**, 3953–3961 (2014)
4. H. Ma, D. Kong, Y. Xu, X. Xie, Y. Tao, Z. Xiao, W. Lv, H.D. Jang, J. Huang, Q.H. Yang, Disassembly-reassembly approach to RuO_2/graphene composites for ultrahigh volumetric capacitance supercapacitor. Small **13**, 1701026 (2017)
5. N. Choudhary, C. Li, J. Moore, N. Nagaiah, L. Zhai, Y. Jung, J. Thomas, Asymmetric supercapacitor electrodes and devices. Adv. Mater **29**, 1605336 (2017)
6. M. Yu, Z. Wang, Y. Han, Y. Han, Y. Tong, X. Lu, S. Yang, Recent progress in the development of anodes for asymmetric supercapacitors. J. Mater. Chem. A **4**, 4634–4658 (2016)
7. J.G. Wang, F. Kang, B. Wei, Engineering of MnO_2-based nanocomposites for high-performance supercapacitors. Prog. Mater. Sci. **74**, 51–124 (2015)
8. J.G. Wang, H. Liu, H. Liu, W. Hua, M. Shao, Interfacial constructing flexible V_2O_5@polypyrrole core-shell nanowire membrane with superior supercapacitive performance. ACS Appl. Mater. Interfaces **10**, 18816–18823 (2018)
9. J.G. Wang, Z. Zhang, X. Zhang, X. Yin, X. Li, X. Liu, F. Kang, B. Wei, Cation exchange formation of prussian blue analogue submicroboxes for high-performance Na-ion hybrid supercapacitors. Nano Energy **39**, 647–653 (2017)
10. M. Hughes, G.Z. Chen, M.S. Shaffer, D.J. Fray, A.H. Windle, Electrochemical capacitance of a nanoporous composite of carbon nanotubes and polypyrrole. Chem. Mater. **14**, 1610–1613 (2002)
11. Q. Wu, Y. Xu, Z. Yao, A. Liu, G. Shi, Supercapacitors based on flexible graphene/polyaniline nanofiber composite films. ACS Nano **4**, 1963–1970 (2010)
12. K. Sun, S. Yu, Z. Hu, Z. Li, G. Lei, Q. Xiao, Y. Ding, Oxygen-containing hierarchically porous carbon materials derived from wild jujube pit for high-performance supercapacitor. Electrochim. Acta **231**, 417–428 (2017)
13. L. Zhang, R. Chen, K.N. Hui, K.S. Hui, H. Lee, Hierarchical ultrathin NiAl layered double hydroxide nanosheet arrays on carbon nanotube paper as advanced hybrid electrode for high performance hybrid capacitors. Chem. Eng. J. **325**, 554–563 (2017)
14. H. Su, H. Zhang, F. Liu, F. Chun, B. Zhang, X. Chu, H. Huang, W. Deng, B. Gu, H. Zhang, X. Zheng, M. Zhu, W. Yang, High power supercapacitors based on hierarchically porous sheet-like nanocarbons with ionic liquid electrolytes. Chem. Eng. J. **322**, 73–81 (2017)
15. P.J. Hall, M. Mirzaeian, S.I. Fletcher, F.B. Sillars, A.J.R. Rennie, G.O. Shitta-Bey, G. Wilson, A. Crunden, R. Carter, Energy storage in electrochemical capacitors: designing functional materials to improve performance. Energy Environ. Sci. **3**, 1238–1251 (2010)
16. M. Guo, J. Guo, D. Jia, H. Zhao, Z. Sun, X. Song, Y. Li, Coal derived porous carbon fibers with tunable internal channels for flexible electrodes and organic matter absorption. J. Mater. Chem. A **3**, 21178–21184 (2015)
17. K.H. Iessa, Y. Zhang, G. Zhang, F. Xiao, S. Wang, Conductive porous sponge-like ionic liquid-graphene assembly decorated with nanosized polyaniline as active electrode material for supercapacitor. J. Power Sources **302**, 92–97 (2016)
18. G.A. Ferrero, A.B. Fuertes, M. Sevilla, From soybean residue to advanced supercapacitors. Sci. Rep. **5**, 16618–16631 (2015)
19. Q. Liang, L. Ye, Z.H. Huang, Q. Xu, Y. Bai, F. Kang, Q. Yang, A honeycomb-like porous carbon derived from pomelo peel for use in high-performance supercapacitors. Nanoscale **6**, 13831–13837 (2014)
20. E.M. Lotfabad, J. Ding, K. Cui, A. Konhandehghan, W.P. Kalisvaart, M. Hazelton, D. Mitlin, High-density sodium and lithium ion battery anodes from banana peels. ACS Nano **8**, 7115–71129 (2014)
21. Y. Zhang, S. Liu, X. Zheng, X. Wang, Y. Xu, H. Tang, F. Kang, Q.H. Yang, J. Luo, Biomass organs control the porosity of their pyrolyzed carbon. Adv. Funct. Mater. **27**, 1604687 (2017)
22. R. Wang, P. Wang, X. Yan, J. Lang, C. Peng, Q. Xue, Promising porous carbon derived from celtuce leaves with outstanding supercapacitance and CO_2 capture performance. ACS Appl. Mater. Interfaces **4**, 5800 (2012)
23. K. Wang, Y. Song, R. Yan, N. Zhao, X. Tian, X. Li, Q. Guo, Z. Liu, High capacitive performance of hollow activated carbon fibers derived from willow catkins. Appl. Surf. Sci. **394**, 569–577 (2017)
24. X. Liu, Y. Zhou, W. Zhou, L. Li, S. Huang, S. Chen, Biomass-derived nitrogen self-doped porous carbon as effective metal-free catalysts for oxygen reduction reaction. Nanoscale **7**, 6136–6142 (2015)
25. T.E. Rufford, D. Hulicova-Jurcakova, Z. Zhu, G.Q. Lu, Nanoporous carbon electrode from waste coffee beans for high performance supercapacitors. Electrochem. Commun. **10**, 1594–1597 (2008)
26. D. Shan, J. Yang, W. Liu, J. Yan, Z. Fan, Biomass-derived three-dimensional honeycomb-like hierarchical structured carbon for ultrahigh energy density asymmetric supercapacitors. J. Mater. Chem. A **4**, 13589–13602 (2016)
27. P. Cheng, S. Gao, P. Zang, X. Yang, Y. Bai, H. Xu, Z. Liu, Z. Lei, Hierarchically porous carbon by activation of shiitake mushroom for capacitive energy storage. Carbon **93**, 315–324 (2015)
28. D. Wang, S. Liu, G. Fang, G. Geng, J. Ma, From trash to treasure: direct transformation of onion husks into three-dimensional interconnected porous carbon frameworks for high-performance supercapacitors in organic electrolyte. Electrochim. Acta **216**, 405–411 (2016)
29. M.A. Islam, M.J. Ahmed, W.A. Khanday, M. Asif, B.H. Hameed, Mesoporous activated carbon prepared from NaOH activation of rattan (*Lacosperma secundiflorum*) hydrochar for methylene blue removal. Ecotoxicol. Environ. Saf. **138**, 279–285 (2017)

30. Y. Zhang, X. Liu, S. Wang, L. Li, S. Dou, Bio-nanotechnology in high-performance supercapacitors. Adv. Energy Mater **7**, 1700592 (2017)
31. C. Su, C. Pei, B. Wu, J. Qian, Y. Tan, Highly doped carbon nanobelts with ultrahigh nitrogen content as high-performance supercapacitor materials. Small **13**, 1700834–1700846 (2017)
32. K.S.W. Sing, D.H. Everett, R. Haul, L. Moscou, R.A. Pierotti, J. Rouquerol, T. Siemieniewska, Reporting physisorption data for gas/solid systems with special reference to the determination of surface area and porosity. Pure Appl. Chem. **57**, 603–619 (1985)
33. L. Sun, C. Tian, M. Li, X. Meng, L. Wang, R. Wang, J. Yin, H. Fu, From coconut shell to porous graphene-like nanosheets for high-power supercapacitors. J. Mater. Chem. A **1**, 6462–6470 (2013)
34. Y.C. Liu, B.B. Huang, X.X. Lin, Z.L. Xie, Biomass-derived hierarchical porous carbons: boosting the energy density of supercapacitors via an ionothermal approach. J. Mater. Chem. A **5**, 13009–13018 (2017)
35. O. Barbieri, M. Hahn, A. Herzog, R. Kötz, Capacitance limits of high surface area activated carbons for double layer capacitors. Carbon **43**, 1303–1310 (2005)
36. W. Qian, F. Sun, Y. Xu, L. Qiu, C. Liu, S. Wang, F. Yan, Human hair-derived carbon flakes for electrochemical supercapacitors. Energy Environ. Sci. **7**, 379–386 (2014)
37. P.S. Yang, L. Ma, M.Y. Gan, Y. Lei, X.L. Zhang, M. Jin, G. Fu, Preparation and application of PANI/N-doped porous carbon under the protection of ZnO for supercapacitor electrode. J. Mater. Sci.: Mater. Electron. **28**, 7333–7342 (2017)
38. F. Sun, J. Gao, X. Liu, X. Pi, Y. Yang, S. Wu, Porous carbon with a large surface area and an ultrahigh carbon purity via templating carbonization coupling with KOH activation as excellent supercapacitor electrode materials. Appl. Surf. Sci. **387**, 857–863 (2016)
39. W. Tian, Q. Gao, W. Qian, Interlinked porous carbon nanoflakes derived from hydrolyzate residue during cellulosic bioethanol production for ultrahigh-rate supercapacitors in nonaqueous electrolytes. ACS Sustain. Chem. Eng. **5**, 1297–1305 (2016)
40. T. Wei, X. Wei, Y. Gao, H. Li, Large scale production of biomass-derived nitrogen-doped porous carbon materials for supercapacitors. Electrochim. Acta **169**, 186–194 (2015)
41. D. Ma, G. Wu, J. Wan, F. Ma, W. Geng, S. Song, Oxygen-enriched hierarchical porous carbon derived from biowaste sunflower heads for high-performance supercapacitors. RSC Adv. **5**, 107785–107792 (2015)
42. W. Tian, Q. Gao, Y. Tan, Z. Li, Unusual interconnected graphitized carbon nanosheets as the electrode of high-rate ionic liquid-based supercapacitor. Carbon **119**, 287–295 (2017)
43. I.I.G. Inal, S.M. Holmes, A. Banford, Z. Aktas, The performance of supercapacitor electrodes developed from chemically activated carbon produced from waste tea. Appl. Surf. Sci. **357**, 696–703 (2015)
44. M. Gopiraman, D. Deng, B. Kim, I. Chung, I.S. Kim, Three-dimensional cheese-like carbon nanoarchitecture with tremendous surface area and pore construction derived from corn as superior electrode materials for supercapacitors. Appl. Surf. Sci. **409**, 52–59 (2017)
45. Y.Q. Zhao, M. Lu, P.Y. Tao, Y.J. Zhang, X.T. Gong, Z. Yang, G.Q. Zhang, H.L. Li, Hierarchically porous and heteroatom doped carbon derived from tobacco rods for supercapacitors. J. Power Sources **307**, 391–400 (2016)
46. D.H. Jurcakova, M. Seredych, G.Q. Lu, T.J. Bandosz, Combined effect of nitrogen-and oxygen-containing functional groups of microporous activated carbon on its electrochemical performance in supercapacitors. Adv. Funct. Mater. **19**, 438–447 (2009)
47. Z. Li, Z. Xu, X. Tan, H. Wang, C.M.B. Holt, T. Stephenson, B.C. Olsen, D. Mitlin, Mesoporous nitrogen-rich carbons derived from protein for ultra-high capacity battery anodes and supercapacitors. Energy Environ. Sci. **6**, 871–878 (2013)
48. A. Izadinajafabadi, S. Yasuda, K. Kobashi, T. Yamada, D.N. Futaba, H. Hatori, M. Yumura, S. Iijima, K. Hata, Extracting the full potential of single-walled carbon nanotubes as durable supercapacitor electrodes operable at 4 V with high power and energy density. Adv. Mater. **22**, 235–241 (2010)
49. H. Li, D. Yuan, C. Tang, S. Wang, J. Sun, Z. Li, T. Tang, F. Wang, H. Gong, C. He, Lignin-derived interconnected hierarchical porous carbon monolith with large areal/volumetric capacitances for supercapacitor. Carbon **100**, 151–157 (2016)
50. E. Redondo, J. Carretero-González, E. Goikolea, J. Ségalini, R. Mysyk, Effect of pore texture on performance of activated carbon supercapacitor electrodes derived from olive pits. Electrochim. Acta **160**, 178–184 (2015)
51. J.G. Wang, H. Liu, H. Sun, W. Hua, H. Wang, X. Liu, B. Wei, One-pot synthesis of nitrogen-doped ordered mesoporous carbon spheres for high-rate and long-cycle life supercapacitors. Carbon **127**, 85–92 (2018)
52. J.G. Wang, H. Liu, X. Zhang, X. Li, X. Liu, F. Kang, Green synthesis of hierarchically porous carbon nanotubes as advanced materials for high-efficient energy storage. Small **14**, 1703950 (2018)
53. D. Guo, X. Chen, Z. Fang, Y. He, C. Zheng, Z. Yang, K. Yang, Y. Chen, S. Huang, Hydrangea-like multi-scale carbon hollow submicron spheres with hierarchical pores for high performance supercapacitor electrodes. Electrochim. Acta **176**, 207–214 (2015)
54. B. Liu, Y. Liu, H. Chen, H. Li, Oxygen and nitrogen co-doped porous carbon nanosheets derived from perilla frutescens, for high volumetric performance supercapacitors. J. Power Sources **341**, 309–317 (2017)
55. E. Raymundo-Piñero, M. Cadek, F. Béguin, Tuning carbon materials for supercapacitors by direct pyrolysis of seaweeds. Adv. Funct. Mater. **19**, 1032–1039 (2010)